



King Saud University
Arabian Journal of Chemistry

www.ksu.edu.sa
www.sciencedirect.com



ORIGINAL ARTICLE

Paper flower-derived porous carbons with high-capacitance by chemical and physical activation for sustainable applications

Pitchaimani Veerakumar^{a,b,*}, Thandavarayan Maiyalagan^{c,*},
Balasubramaniam Gnana Sundara Raj^c, Kuppuswamy Guruprasad^c,
Zhongqing Jiang^d, King-Chuen Lin^{a,b,*}

^a Department of Chemistry, National Taiwan University, Taipei 10617, Taiwan

^b Institute of Atomic and Molecular Sciences, Academia Sinica, Taipei 10617, Taiwan

^c Electrochemical Energy Laboratory, Department of Chemistry, SRM Institute of Science and Technology, Kattankulathur 603203, India

^d Department of Physics, Key Laboratory of ATMMT Ministry of Education, Zhejiang Sci-Tech University, Hangzhou 310018, China

Received 2 July 2018; accepted 18 August 2018

KEYWORDS

Porous carbon;
Supercapacitor;
Adsorption;
Sunset yellow;
Adsorption capacity

Abstract Porous carbon nanosheets were prepared by the carbonization of paper flower via chemical and physical activation. The structural properties of the as-prepared carbons were characterized using the techniques, such as X-ray diffraction (XRD), Fourier-transform infrared spectroscopy (FT-IR), Raman spectroscopy, N₂ sorption isotherms and X-ray photoelectron spectroscopy (XPS), while the related morphological analyses were conducted using scanning/transmission electron microscopy (SEM/TEM). The obtained carbons exhibit a high specific surface area up to 1801 m² g⁻¹ with a robust porous graphitic carbon layer structure, which provides the merits for potential application in energy storage and dye removal. We carried out potentiostatic and galvanostatic measurements using a three-electrode cell in 1.0 M H₂SO₄ aqueous electrolyte and achieved a specific capacitance of 118, 109.5, 101.7, 93.6, and 91.2 F g⁻¹ at 1, 2, 4, 8 and 12 A g⁻¹, respectively. The stability at 12 A g⁻¹ was tested to reach 10,000 cycles with capacity retention of around 97.4%. We have demonstrated that the paper flower-derived carbons at activation temperature 800 °C

* Corresponding authors.

E-mail addresses: spveerakumar@gmail.com (P. Veerakumar), maiyalagan@gmail.com (T. Maiyalagan), kcclin@ntu.edu.tw (K.-C. Lin).
Peer review under responsibility of King Saud University.



Production and hosting by Elsevier

<https://doi.org/10.1016/j.arabjc.2018.08.009>

1878-5352 © 2018 Production and hosting by Elsevier B.V. on behalf of King Saud University.

This is an open access article under the CC BY-NC-ND license (<http://creativecommons.org/licenses/by-nc-nd/4.0/>).

Please cite this article in press as: Veerakumar, P. et al., Paper flower-derived porous carbons with high-capacitance by chemical and physical activation for sustainable applications. Arabian Journal of Chemistry (2018), <https://doi.org/10.1016/j.arabjc.2018.08.009>

(PFC-800) can be used as a promising electrode material in supercapacitor. PFC-800 can also serve as an efficient sunset yellow dye removal, showing the maximum adsorption capacity for sunset yellow (Q_0 , 273.6 mg g⁻¹).

© 2018 Production and hosting by Elsevier B.V. on behalf of King Saud University. This is an open access article under the CC BY-NC-ND license (<http://creativecommons.org/licenses/by-nc-nd/4.0/>).

1. Introduction

Biomass resources have recently drawn much attention as carbon precursors to derive activated carbons (ACs), mainly due to renewability and environmental friendliness (Peng et al., 2013; Long et al., 2015) as compared with traditional bio-sources such as protein (Li et al., 2013), wood (Guo et al., 2017), and corncob (Wang et al., 2015). The essential requirement for the carbon precursor in the application of electrochemical energy storage is to generate carbons with large surface areas and pore volumes (He et al., 2013). Therefore, the activation process followed by carbonization treatment is usually required to increase surface area and micro/mesoporosities of ACs (Zhao et al., 2010). The common chemical activating agents such as KOH, H₃PO₄, ZnCl₂, etc have been used to enhance the textural properties like surface area (> 3000 m² g⁻¹), pore volume and tailorable pore size (Wang and Kaskel, 2012). Due to such unique merits, ACs are successfully utilized for hydrogen storage (Yu et al., 2017), adsorption (Veerakumar et al., 2017), electrochemical sensors (Yao et al., 2017) and supercapacitor (SC) applications (Veerakumar et al., 2018).

Till now, SCs serves as one of most charming electrochemical charge-storage devices; it offers many prospective applications in the field of hybrid electric vehicles, telecommunications, portable electronics, security alarm systems, uninterruptible power supply (UPS), and solar power systems (Lu et al., 2017; Zhang et al., 2017; Li et al., 2018). Numerous porous carbon nanomaterials have been developed for SC applications, such as graphene (Yang et al., 2017), activated carbons (Borenstein et al., 2017), carbon nanotube (Zheng et al., 2017; Tian et al., 2018), carbon fibers (Chen et al., 2017), carbon aerogels (Han et al., 2017), and polymers (Shi et al., 2015). Currently, graphene nanomaterials exhibit unique distinct features and widely used to form supercapacitors, but the preparation of graphene or graphene oxide is an intricate procedure that may lead to hazardous explosions (Zaaba et al., 2017). On the other hand, despite carbon nanotubes and buckminsterfullerene showing a moderate surface area and good conductivity, the as-prepared supercapacitors do not achieve good capacitive performance; manufacturing difficulties and the cost restrict their applications in energy storage devices (Zheng et al., 2017; Tian et al., 2018). As reported, the specific surface area of carbon fibers, carbon aerogels, and polymers ranges from 500 to 1000 m² g⁻¹, of which only a fraction can be used for energy storage; the difficulty to tune the porous structure further restricts their large-scale production and practical applications (Li et al., 2017; Zhu et al., 2018).

Among these carbon sources, ACs has recently attracted wide attention because of low cost, environmental benignity, and well-defined pore structures and topologies. The procedure for fabrication of ACs from biomass precursors is simple and renewable. Further, the resulting porous ACs can provide

a large specific surface area, high porosity, chemical, thermal, and structural stability, natural presence of desirable surface oxygen functional groups and favorite pathways for the ion diffusion (Sevilla and Fuertes, 2014; Shi et al., 2017; Kang et al., 2018). A large amount of natural plant and animal/insect wastes are treated as renewable carbon sources which have drawn increasing interest in both fundamental research and industrial applications (Biswal et al., 2013; Gao et al., 2014; Panmand et al., 2017).

Herein we report the preparation of porous carbon nanosheets derived from *Bougainvillea Spectabilis* biowaste for high-performance SCs. *Bougainvillea Spectabilis* is sometimes known as “paper flower (PF)” because the bracts are thin and papery. PF is a fast-growing plant and reported to have medicinal values including antidiabetic properties (Khairy et al., 2016). It mainly consists of betanin (natural dye), a saccharide (betanidin, betaxanthin) and lignocellulosic fibers, etc., which should be beneficial to the synthesis of ACs because of their high levels of a saccharide type cellulose, and fine fibrous networks present in the paper flowers (Isah et al., 2015). Therefore, paper flower carbons (PFC) are likely to become the promising electrode materials for SC as well as for removal of sunset yellow (SY) dye from aqueous solution. The overall preparation procedure is illustrated in Scheme 1.

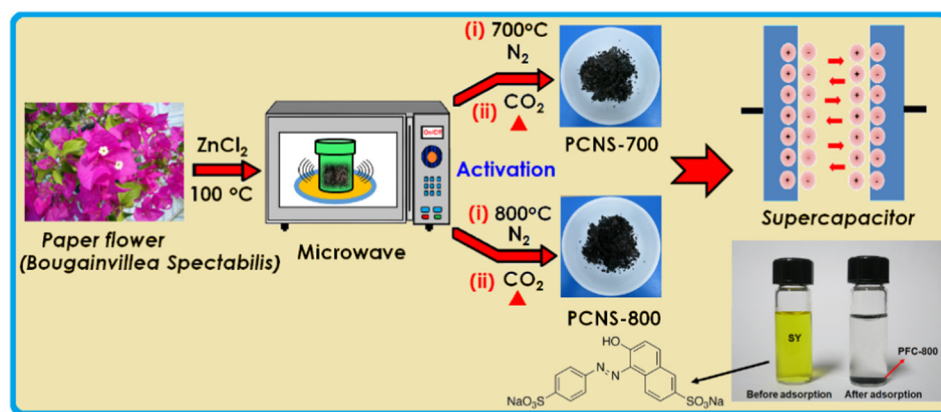
2. Experimental section

2.1. Materials

Paper flowers (*Bougainvillea Spectabilis*) were collected from the campus of National Taiwan University. Vulcan XC-72, polyvinylidene fluoride (PVDF), *N*-methyl-2-pyrrolidone (NMP) and sunset yellow FCF (SY) were purchased from Fluka and Merck, respectively. All chemicals were used after purchase. All the solutions were prepared using ultrapure water (MilliQ, 18.25 MΩ cm).

2.2. Preparation of activated carbon

The mature paper flower (PF) was collected after they fell from (*Bougainvillea Spectabilis*) plants. The pre-cleaned PFs were ground to small particles (<2.0 mm) from which the PF-derived carbons (PFC) products were generated while placed in a tubular furnace through the carbonization and subsequent activation process. Typically, ~2 g PFs were impregnated in 100 mL of ZnCl₂ aqueous solution corresponding to a ratio of ZnCl₂: PFs = 3:1 by weight. After 24 h of impregnation, the PFs was placed under microwave (mw) irradiation (Milestone's START MW power: 300 W) at a rate of 10 °C min⁻¹ to reach 100 °C at which the treatment then lasted for 6 h. The obtained slurry-like carbon materials were collected, washed thoroughly with 3 M HCl and deionized water



Scheme 1 Illustration of the preparation route for PFC carbon for supercapacitor and dye removal applications.

(until a neutral pH), and then dried at 100 °C for 2 h. Subsequently, 0.5 g PFs carbon products were placed in a horizontal transparent tube furnace (Y02PB, Thermacraft Inc., USA) under N₂ atmosphere and heated to the different temperature (700 or 800 °C) at a rate of 5 °C min⁻¹ for graphitization treatment. Then, this maximum temperature (700 or 800 °C) remained for 1 h prior to switching to CO₂ activation with a flow rate 30 mL min⁻¹ at the same temperature for 30 min. Finally, the resultant carbon powders, denoted as PFC-*x* where *x* is the activation temperatures (400, 700 and 800 °C).

2.3. Material characterizations

X-ray diffraction (XRD) data were obtained on a PANalytical X'Pert PRO diffractometer using Cu K α radiation generator. Scanning electron microscopy (SEM) images were obtained using a field-emission scanning electron microscope (SEM; JEOL JSM-6500F) and field-emission transmission electron microscopy (FE-TEM) images were obtained using a field-emission TEM (JEM2100F, JEOL) operated at 200 kV. The structure was examined using Raman scattering spectroscopy (Jobin Yvon T64000 spectrometer). X-ray photoelectron spectroscopy (XPS) data were obtained using ULVAC-PHI PHI 5000 VersaProb apparatus. N₂ adsorption/desorption isotherm was performed on the Autosorb-1 surface analyzer and the evaluation of specific surface area of different samples was based on Brunauer-Emmett-Teller analysis. The functional groups of the as-prepared carbons were determined by FT-IR analysis in a Bruker IFS28 spectrometer with a KBr pellet. Thermo-gravimetric analyzer (TGA) was used to account for the weight change of the samples when exposed to high temperature recorded. The TGA data were measured using Netzsch TG-209 at 25–900 °C with 10 °C min⁻¹ of heating rate under ambient condition.

2.4. Electrochemical tests

The electrochemical impedance spectroscopy (EIS) from 100 KHz to 10 MHz controlled at 10 mV amplitude, cyclic voltammetry (CV), galvanostatic charge/discharge measurements (GCD), and cycling performance were evaluated using a SP 300-EC-Lab testing system. The working electrode for electrochemical tests was prepared by coating slurry (PFC),

75 wt%, Vulcan XC-72 (20 wt%), PVDF (5 wt%)) onto a grade-304 stainless steel (SS) plate as current collectors and then dried at 65 °C under vacuum oven for 12 h. Electrochemical properties of individual electrodes were evaluated using a three-electrode cell with Pt foil as the counter electrode, PFC coated SS plate as the working electrode and Ag/AgCl as the reference electrode with 1 M H₂SO₄ electrolyte. We then selected a potential window from -0.1 to +0.9 V for the CV and GCD measurements, in which CV was operated at different scan rates of 10, 20, 40, 80, 160 and 320 mV s⁻¹, while GCD was fixed at a current density of 0.5 mA cm⁻².

All the CV and GCD experiments were performed on an electrochemical workstation. The specific capacitance (SC, F g⁻¹) of the sample electrodes was calculated using Eq. (1) for CV measurements (Wahid et al., 2014).

$$SC = \frac{Q}{m\Delta V} \quad (1)$$

where *Q* is the average charge during the charge and discharge process (C), *m* the mass (g), and ΔV the working potential (V). The following equation is for the GCD measurements (Zhou et al., 2015).

$$SC = \frac{I\Delta t}{m\Delta V} \quad (2)$$

where *I* is the applied current density (A g⁻¹), Δt the discharge time (s), and ΔV the voltage window after iR drop.

3. Results and discussion

3.1. Physical characterization

During the physicochemical activation process, the functional groups after carbonization at different temperature can be usually verified using FT-IR spectroscopy. Hence, we employed FTIR spectrometer to analyze the cleaned and dried PFs products during the heating process of ZnCl₂-impregnated PFs from room temperature to 800 °C. Fig. 1a shows several characteristic peaks for the pre-carbonized PFs at room temperature, indicating their complicated chemical structure. A broad peak at 3433 cm⁻¹ was ascribed to the hydroxyl (—OH) stretching and the peak at 3011 cm⁻¹ was assigned to the stretching of C—H benzene rings. The three peaks at

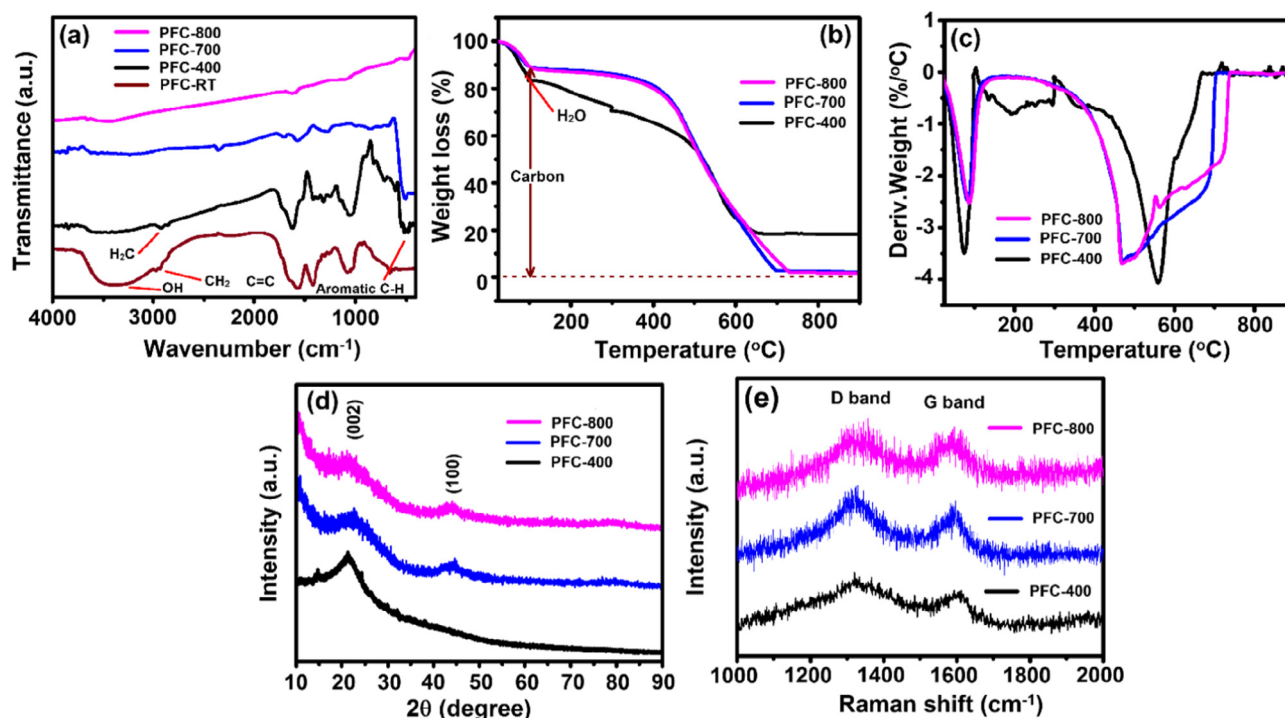


Fig. 1 (a) FT-IR spectra, (b) TGA curves, (c) DTA curves, (d) XRD patterns and (e) Raman spectra of the PFC.

1608, 1501 and 1452 cm^{-1} were characteristic of the C=C in benzene rings (Dominguez et al., 2013). The peak at 752 cm^{-1} was ascribed to disubstituted-1,2 in the aromatic rings, while the peaks at 878 and 818 cm^{-1} corresponded to 1,2,4-substitutions and 1,4-substitutions, respectively. Meanwhile, the stretching of a phenolic hydroxyl group, C—O—, and a hydroxymethyl group was identified by inspecting the peaks at 1357, 1219 and 1011 cm^{-1} , respectively (Yahya et al., 2015). In addition, the peaks around $400\text{--}600\text{ cm}^{-1}$ contain various bands related to aromatic, out of plane C—H bending with different degrees of substitution (Zhang et al., 2016). Fig. 1a also shows the precursor PFs spectrum activated by ZnCl_2 at $400\text{ }^\circ\text{C}$ for comparison. The peak at 3430 cm^{-1} corresponding to hydroxyl groups became less intense and shifted to a high wavenumber when the activation temperature was raised to $400\text{ }^\circ\text{C}$. Meanwhile, the peak intensities of the C—H stretching at 2920 and 2852 cm^{-1} decreased. The peak for the C=O group at 1735 cm^{-1} disappeared. These changes in FT-IR spectra evidenced that the ZnCl_2 activation played an importation role to cause catalytic dehydration and condensation reaction between the oxygen-containing functional groups in precursor PFs during the heating process, which diminished hydroxyl, methylene, phenolic hydroxyl and methylol groups (Huang et al., 2016).

As the activation temperature was increased to 700 or $800\text{ }^\circ\text{C}$, the peak at 3430 cm^{-1} became weakly detected, indicating consumption of —OH groups in dehydration reactions (Fig. 1a). At the same time, the C=C vibrations in benzene rings at 1608 and 1450 cm^{-1} became weak, because large amounts of aromatic rings were changed to multi-benzene fused ring structures. The multi-benzene fused ring structure was reported to be an intermediate state when the carbon materials were changed towards a graphite structure in the heating process (Yahya et al., 2015; Huang et al., 2016). There-

fore, as the amount of multi benzene rings increase, the polymerization of carbon netlike structures and the subsequent graphite-like structures may be enhanced to some extent (Yu et al., 2018).

In addition, the weight loss and carbon content of ZnCl_2 -impregnated PFs and pre-carbonized ($400\text{ }^\circ\text{C}$) samples were measured through thermogravimetric analysis (TGA) in the O_2 atmosphere with a heating rate of $10\text{ }^\circ\text{C min}^{-1}$ (Fig. 1b). In the first step, the thermal decomposition of ZnCl_2 -impregnated and pre-carbonized ($400\text{ }^\circ\text{C}$) PFs sample with amorphous carbon structure resulted in the weight loss 8.5 wt% from 45 to $105\text{ }^\circ\text{C}$ due to the moisture release; then, a significant weight loss from 257 to $470\text{ }^\circ\text{C}$ is caused by the complete combustion of non-graphitic carbons and volatiles release which shows two peaks of DTA curve in this range. However, a trace amount of remnant ZnO oxides was found. The last stage from 470 to $900\text{ }^\circ\text{C}$ may result in dehydration and dehydrogenation which occurred persistently in the aromatic ring to form net-like structures of hexatomic rings (Fig. 1c). The decomposition of oxygen-containing groups at high temperatures can still lead to weight loss, but the main reason was due to gasification of ZnCl_2 (b.p $\sim 732\text{ }^\circ\text{C}$) (Hu et al., 2001). In brief, chemically adsorbed water molecules were evaporated below $100\text{ }^\circ\text{C}$. Then, a stable formation was observed up to $400\text{ }^\circ\text{C}$, and finally, an extreme weight loss between 400 and $700\text{ }^\circ\text{C}$ was owing to the decomposition of carbon structure. These results demonstrated that a more stable carbon structure was formed after physicochemical activation process of the PFs.

X-ray diffraction (XRD) data for the PFs derived carbon products at 400, 700 and $800\text{ }^\circ\text{C}$ are displayed in Fig. 1d. The peak at 24.2 is broad with a small intensity, suggesting the amorphous feature of the pre-carbonized carbon at $400\text{ }^\circ\text{C}$. When carbonization temperature increases, two major

diffraction peaks observed at around 22° and 43° correspond to the graphitic (0 0 2) and (1 0 0) planes, respectively, revealing the presence of more graphitic and less disordered carbon, as expected after CO_2 activation (Zickler et al., 2006). No significant peaks assignable to ZnCl_2 or ZnO reveal their high purities of carbon derived from PFs.

Next, Raman spectroscopy was employed to inspect the structures of the PFC samples and to characterize the different types of sp^2 carbon nanostructures. As shown in Fig. 1e, the Raman spectra of pre-carbonized (at 400°C) sample exhibit two broad peaks at 1559 and 2699 cm^{-1} which can be assigned to D (A_{1g} symmetry) and G band (E_{2g} symmetry) of the disordered and ideal graphitic lattice, respectively (Wei et al., 2011). The intensity ratio (I_D/I_G) observed for both samples (PFC-700 and 800) are 0.98 and 0.99 respectively, indicating the similarity with the graphitic structure. It is worthwhile to note that the I_D/I_G values observed at the same graphitization temperature for commercial activated carbons (Knight and White, 1989) and ordered carbon nanosheets (Wang et al., 2013) are 0.52 and 0.90, respectively. The chemical and physical activation treatment does enhance the property for the graphitic structure. Notably, the I_D/I_G value of the as-obtained PFC was estimated as ~ 0.99 , which should be responsible for the desirable electronic conductivity for the SC applications.

Brunauer–Emmett–Teller (BET) nitrogen adsorption/desorption isotherms were acquired to evaluate the porosity and surface area of the activated samples (Fig. 2a). According to the BET isotherm, a very low surface area of $290.1\text{ m}^2\text{ g}^{-1}$ with

a pore volume of $0.067\text{ cm}^3\text{ g}^{-1}$ was evaluated for low temperature activated sample (PFC-400) and the curve shows a type-II isotherm with mesoporous in nature. The BET surface area was determined to be 1700 and $1801\text{ m}^2\text{ g}^{-1}$ for PFC-700 and PFC-800 samples, respectively, indicating the type I isotherms with hysteresis loops characteristic of micro/mesoporous structures (Karnan et al., 2016). The pore size distribution on the basis of BJH analysis (inset of Fig. 2b) is mainly centered at approximately 2–3 nm.

Table 1 presents a summary of the porous structure for the prepared carbons (surface area, pore volume, and pore size), of which PFC-800 sample shows the largest surface area ($S_{\text{BET}} = 1800\text{ m}^2\text{ g}^{-1}$) and the largest pore volume ($V_{\text{Tot}} = 1.16\text{ cm}^3\text{ g}^{-1}$). The suitable pore size and pore volume may supply micro/mesopore channels penetrable for the migration of electrolyte ions, and meanwhile shorten the pathway for the ion motion to facilitate the ion diffusion kinetics. Furthermore, the elemental composition of PFC-400, PFC-700, and PFC-800 was examined by Thermo Flash 2000 CHNS/O Analyzer. Typically, the PFC-400 sample contains carbon (41.01 wt%), hydrogen (5.33 wt%), and oxygen (52.02 wt%). During the pyrolysis process, some volatile matter decomposed into vapors, hence showing a reduced amount of C, H and O elemental composition in the PFC-800. The effect of pyrolysis temperature on product composition is given in Table 1. PFC-800 yielded C amount only with 40.08 wt% at the pyrolysis temperature of 800°C . The H and O contents increased dramatically at the price of decrease of the carbon

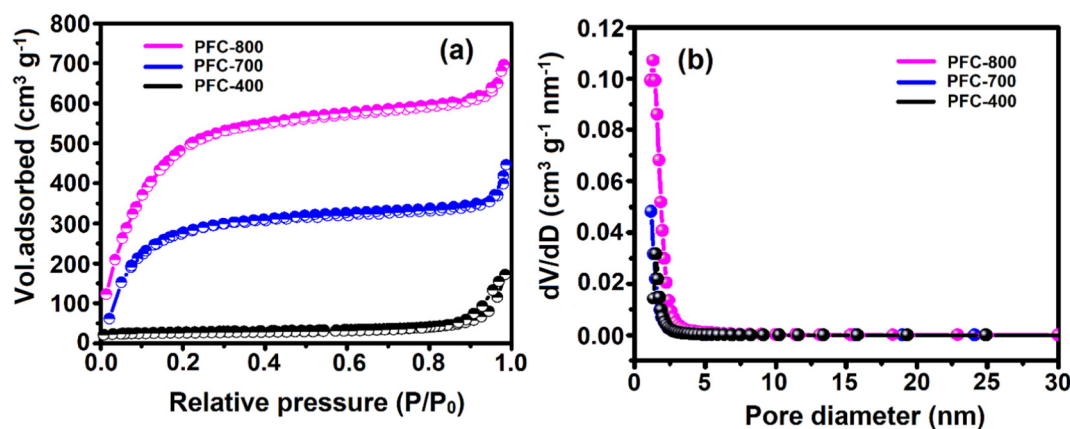


Fig. 2 (a) N_2 adsorption/desorption isotherms, and (b) pore-size distribution of as-prepared PFC.

Table 1 Physical properties of the various as-synthesized samples.

Samples	Surface area ^a ($\text{m}^2\text{ g}^{-1}$)		Pore volume ^b ($\text{cm}^3\text{ g}^{-1}$)			D_p^c (nm)	Elemental analysis (wt%)			I_D/I_G
	S_{Tot}^a	S_{micro}^c	V_{Tot}^b	V_{micro}^c	V_m		C	H	O	
PFC-400	290.1	72.16	0.088	0.011	0.077	2.83	41.01	5.33	52.02	1.01
PFC-700	1700	275.2	0.862	0.227	0.635	3.12	40.27	5.81	52.87	0.98
PFC-800	1801	348.8	1.161	0.553	0.509	3.28	40.08	5.94	52.95	0.99

^aBrunauer–Emmett–Teller (BET) surface areas.

^bTotal pore volume derived from the N_2 uptake at $P/P_0 = 0.99$.

^cMicroporous surface area and pore volume obtained from t -plot analysis.

^dMesoporous volume ($V_{\text{Meso}} = V_{\text{Tot}} - V_{\text{Micro}}$).

^ePore size determined by BJH method.

contents after the treatment of chemical and physical activation, thus indicating successful surface area and pore volume enhancement. The involvement of heteroatoms such as O and H may enhance the electrochemical properties of PFC-800.

The morphology of the PFC-400, PFC-700, and PFC-800 samples were examined using FE-SEM micrographs (Fig. 3), showing the porous nature of carbon which appears like thin sheets and folds on the surface.

The field-emission transmission electron microscopy (FE-TEM) images for the as-prepared PFC-700 and PFC-800 with different magnifications were illustrated in Fig. 4a,b and c-e, respectively. The figures show that the activated PFC have an extensive number of micro/mesopores with interconnected porous carbon matrix, which should facilitate electrolyte exchange. Apparently, the PFC is very thin with lattice fringes like graphene and its SAED spectrum is displayed in Fig. 4f. In addition, typical FE-TEM images of PFC-400 sample (Fig. S3, SI) show the interconnected carbon framework with small

micropores which mostly contain amorphous nature (see Fig. 1d).

The XPS result (Fig. 5a) reveals that the sample contains O and C elements within the range of 0–1000 eV. In Fig. 5b, the XPS pattern for C 1s comprises a major peak at 283.1 eV attributed to the C–C bonds in conjugation with three other less intense peaks with the binding energies (B.E) at 284.3, 285.4 and 287.9 eV, which are assigned to the C–O, C–C=O and π - π^* shake-up satellite bonding, respectively. The O 1s broad spectrum (Fig. 5c) was deconvoluted into three peaks with B.E ca. 529.8 eV (C=O), 531.9 eV (C–O), and 532.8 eV (C–O–C/C–OH). Oxygen-containing functional groups after the activation can be successfully formed from the binding energies of C 1s and O 1s for the PFC-800 as observed in Fig. 5c. XPS study further reveals that chemical/physical activation of porous carbon essentially leads to the formation of large micro/mesopores (Zhang et al., 2018). According to the above results, the PFCs thus prepared are expected to achieve satisfactory electrochemical performance.

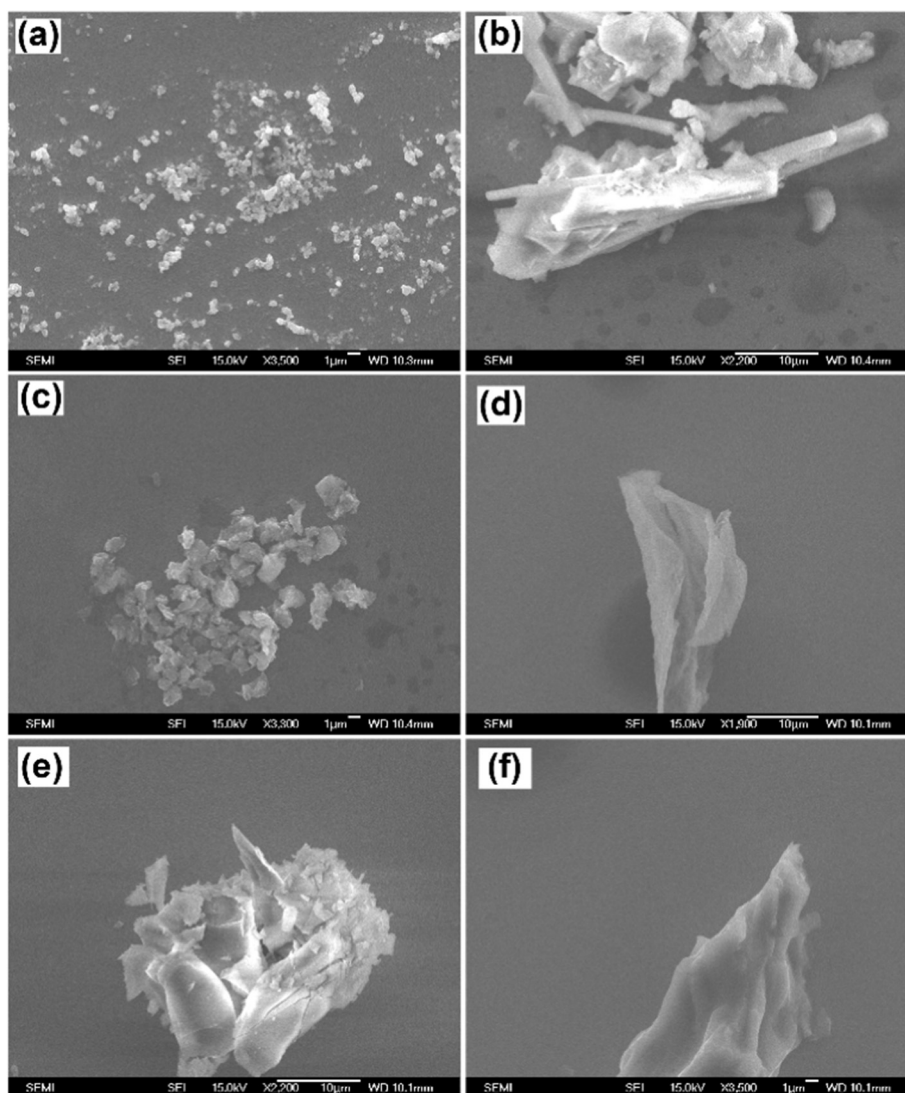


Fig. 3 FE-SEM images of as-prepared (a, b) PFC-400, (c, d) PFC-700, and (e, f) PFC-800 samples.

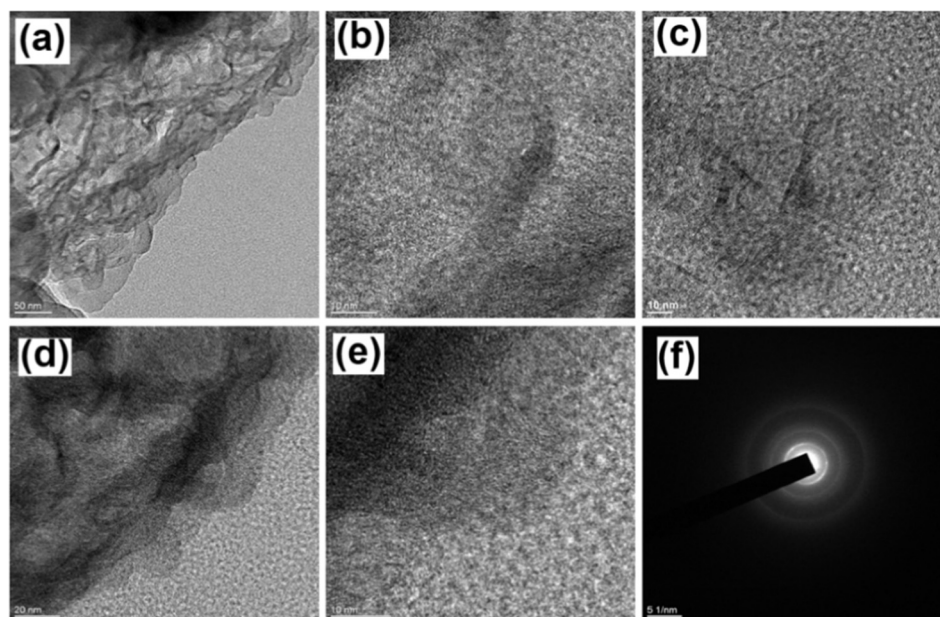


Fig. 4 FE-TEM images of (a, b) PFC-700, (c-e) PFC-800 samples and (f) show the corresponding SAED pattern of PFC-800.

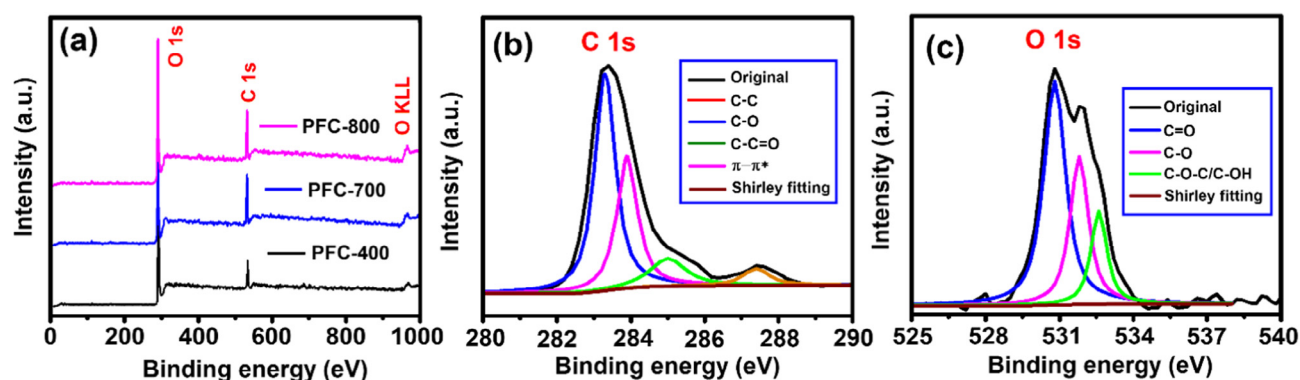


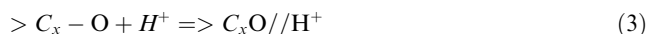
Fig. 5 (a) XPS survey spectra of the PFC-400, PFC-700 and PFC-800 samples, (b) C 1s and (c), O 1s core-level spectra of the PFC-800 sample.

3.2. Electrochemical behavior of the PFC electrode

In recent years, electrochemical capacitors (ECs) have become a new hot spot in the field of energy storage due to their high levels of electrical power, large specific energy density, fast charging-discharging rates and environmental protection (Ratha and Rout, 2013). According to the working mechanisms, supercapacitors can be divided into two types. One is pseudocapacitors, which store energy through physical adsorption; for instance, the pseudocapacitive materials (Jayalakshmi and Balasubramanian, 2008) store energy through a faradaic process, which involves fast and reversible redox reactions between the electrolyte and electroactive materials on the electrode surface (Jiang et al., 2018). In principle, the electroactive species, which possess various valence/oxidation states, have pseudo charge storage abilities. The most widely explored electroactive materials include (i) transition-metal oxides (Zhang and Zhao, 2009), hydroxides, or nitrides (Choi et al., 2006), (ii) conducting polymers (CPs) (Rudge et al., 1994) such as

polyaniline (PANI), polypyrrole (PPy), and polythiophene (PT), and (iii) materials possessing oxygen- and nitrogen-containing surface functional groups (Li et al., 2007; Jeong et al., 2011). The other type is electric double layer capacitors (EDLCs) or non-faradaic supercapacitors, which store energy using the adsorption of both anions and cations. Currently, most of state-of-the-art EDLCs devices are based on high-surface-area carbons such as porous activated carbon (ACs), carbon spheres (CSs), carbon nanotubes (CNTs), graphene (Gr) and so forth owing to the charge separation at the electrolyte interface (Gu et al., 2015). Thus, the as-prepared PFC materials possess the unique structural and textural properties showing a potential application in high-performance EDLCs. The electrochemical application of the PFC materials is then performed to evaluate supercapacitors in a three-electrode cell configuration. In this study, the PFC-400 sample with the limited surface area and the pore volume restricts the electrolyte ions to enter the micropores and thus leading to a decrease of the specific capacitance (Hwang et al., 2017). Besides, the

PFC-400 has a low degree of crystallinity and poor surface area, which impedes the charge transfer and suffers an energy loss in an SCs device (Kinoshita, 1988). Thus, it is necessary to increase surface area or add conductive materials into the carbon to form a composite electrode to increase its conductivity. Hence, the surface structure plays a very crucial role in energy storage systems (Hsieh and Teng, 2002). Thus far, PFC become popular in the device manufacture, by taking advantage of such as their large surface area, relatively high chemical stability, reasonable cost, abundance, biocompatibility, and scalable synthesis (Halama et al., 2010). An activated carbon redox reaction has been proposed for pseudocapacitance in a 1.0 M H_2SO_4 aqueous electrolyte by the following reaction (Eqs. (3) and (4):



where the symbol $>$ represents the surface of the PFC-800 material, and the symbol $//$ denotes the adsorption interface between H^+ and the oxygen functional groups present in the PFC-800. The electron transfer process is expressed by (Zhang et al., 2014).



This reaction formula indicates that the proton H^+ is not only adsorbed on the oxygen functional groups, but also involved in the electron transfer. In performance of the electro-

chemical behavior, cyclic voltammetry (CV) of PFC at a potential window of -0.1 to $+0.9$ V with 20 mV s^{-1} is demonstrated in Fig. 6a. The CV measurements for both samples appear to have rectangular-like shape with mirror image characteristics but without showing any redox peaks. From the results, an effective EDLC behavior can be inferred for the as-prepared samples. Generally, the total area under CV curve is directly related to specific capacitance. The CV curve area for PFC-800 is found to be larger than PFC-700. This indicates that the former sample has relatively larger capacitance, because of enhancement of surface area and the porosity of the material.

Fig. 6b shows the CV for PFC-800 at a scan rate from 10 to 320 mV s^{-1} in the same potential range vs. Ag/AgCl. Notably, the voltammetric current is found to vary linearly with the scan rate, suggesting its direct dependence on the scan rate (Raj et al., 2015a,b). At a reduced scan rate, H^+ ions may fill up most of the active sites on the surface as well as interior regions of PFC electrode. This may be due to the fact that the electrochemical adsorption-desorption process at lower scan rate has sufficient time for ion diffusion. In contrast, at higher scan rate, the ions are unable to acquire sufficient time for their efficient diffusion into the active sites due to their high mobility rate (Das et al., 2017). The rectangular shape remains similar even when the scan rate is increased to 320 mV s^{-1} , suggesting a good efficiency for electrochemical performance and low

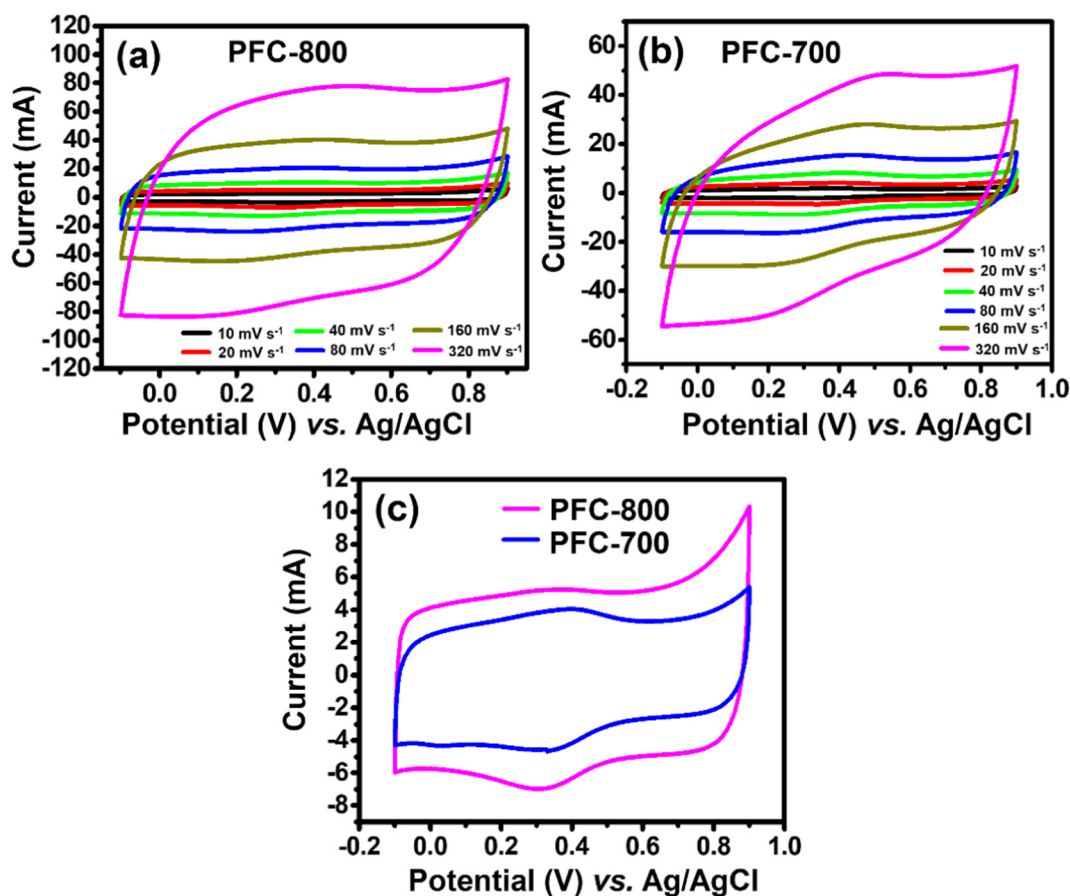


Fig. 6 (a) CV curves of PFC-800 and (b) PFC-700-modified electrodes at various scan rates in the potential range of -0.1 to $+0.9$ V vs. Ag/AgCl in aqueous media (1.0 M H_2SO_4 solution as an electrolyte), and (c) CV curves of PFC-700 and PFC-800 modified electrode with a scan rate 20 mV s^{-1} .

equivalent series resistance of the electrode. As shown in Fig. 6c, nearly perfect rectangular-shaped loop was obtained at 20 mV s^{-1} from -0.1 to $+0.9 \text{ V}$ range without any redox peaks, indicating that the PFC-800 electrode tends to work as a typical EDLC formation.

The examinations of the rate capability and cycling performance further highlight the significant role of the PFC acting for the high-performance supercapacitors. To get further insight into the capacitive behavior, the charge/discharge and cycling abilities were studied. Fig. 7a and Fig. 7b illustrates the GCD patterns of PFC-800 and PFC-700 modified electrode at 1, 2, 4, 8 and 12 A g^{-1} in $1.0 \text{ M H}_2\text{SO}_4$ in the voltage window of -0.1 to 0.9 V (vs. Ag/AgCl). The potential was found to be directly proportional to the time during charging/discharging, which can be another indication for the capacitor. The adsorption-desorption at the electrode/electrolyte interface mainly accounts for the capacitive performance. Obviously, a longer discharge time possessed by PFC-800 indicates that the higher capacitance of the PFC-800 with respect to PFC-700 electrode. The specific capacitance was estimated utilizing the above-mentioned mathematical identity (see Eqn (2); Huang et al., 2012).

Fig. 7c shows the comparison of GCD patterns between PFC-800 and PFC-700 at a high current density of 12 A g^{-1} . The specific capacitances of PFC-700 and PFC-800 electrodes were calculated to be 44.9 F g^{-1} and 91.2 F g^{-1} at 12 A g^{-1} .

Since the capacitance stability with increasing charge-discharge cycles is the prerequisite for an effective capacitive performance, an analysis highlighting specific capacitance values with respect to the charge/discharge cycle numbers is carried out as presented in Fig. 7d. At the 5400th cycle, there was only slight fading of about 1.3% from its starting capacitance value. Even after consecutive charge/discharge operations up to 10,000 cycles, a high stability in cycling performance can be predicted with fading of only 8.6% in the specific capacitance. After 10,000 cycles a capacitance of 88.8 F g^{-1} is achieved showing a stable retention value of 97.4%. The results reveal that the prepared electrode using porous carbon PFC-800 presented an excellent capacitive behavior.

Furthermore, electrochemical impedance spectroscopy (EIS) measurements were conducted to understand the PFC capacitive behavior from 100 KHz to 10 MHz alternating current frequency range with an open-circuit condition (Fig. 8). Fig. 8a shows the Nyquist plots for PFC-700 and PFC-800 electrodes with an amplitude of 10 mV . At high-frequency range, a semicircle is observed for both electrodes, while a vertical region can be visualized at low-frequency range which indicates pure capacitive performance for both the electrodes. The charge transfers resistance (R_{ct}) which mainly occurs at electrode/electrolyte interface at high frequency is represented by the semicircle diameter (Huang et al., 2012). The smaller semicircle in PFC-800 indicates a massive decrement in R_{ct} .

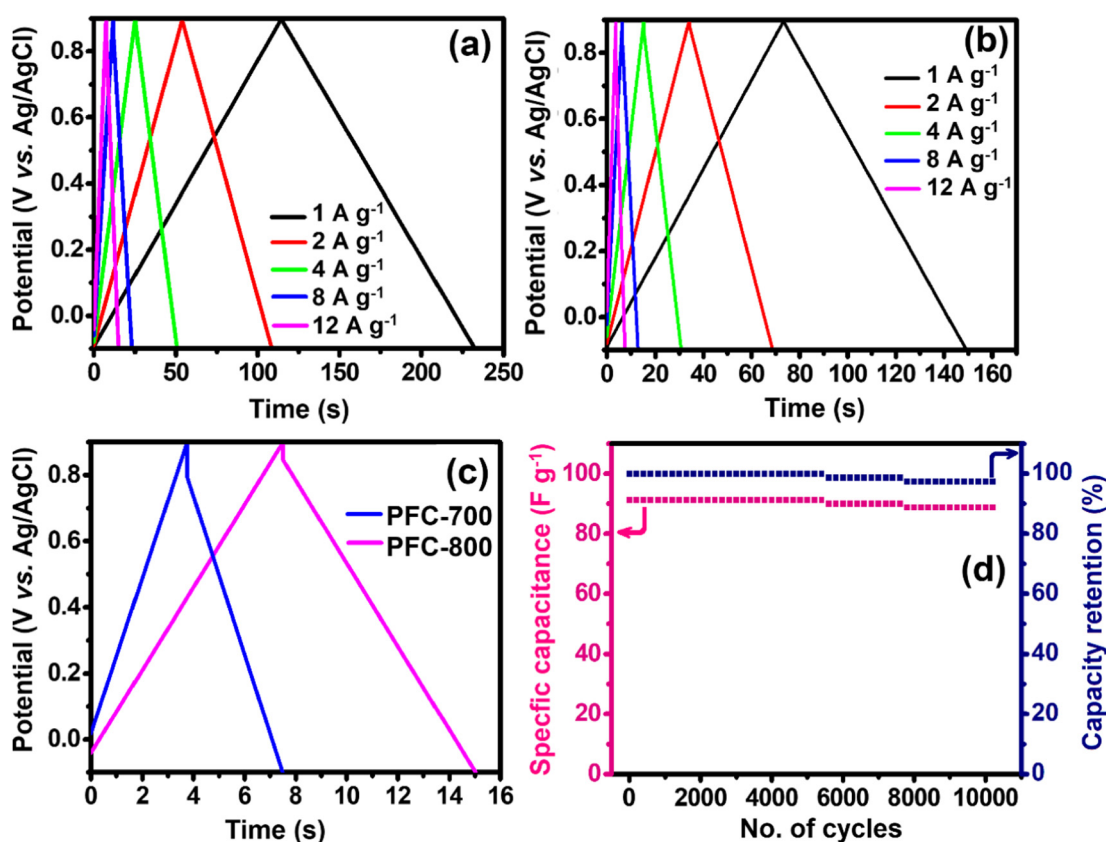


Fig. 7 GCD curves of (a) PFC-800 and (b) PFC-700-modified electrodes with different current density, (c) comparison of GCD curves of PFC-700 and PFC-800-modified electrodes at higher current density of 12 A g^{-1} , and (d) cyclic performance and capacitance retention of PFC-800 electrode. All the cycling performance measured by using a three-electrode system in $1.0 \text{ M H}_2\text{SO}_4$ and potential range from -0.1 to $+0.9 \text{ V}$.

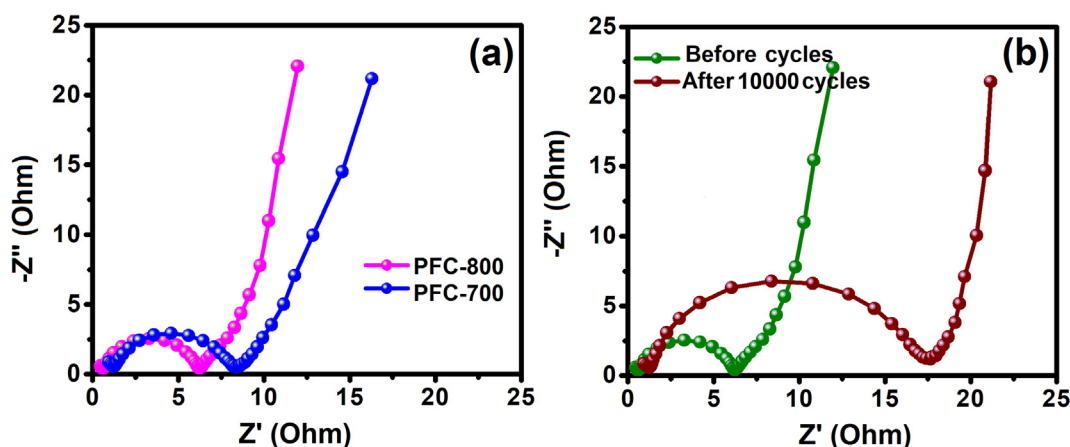


Fig. 8 (a) EIS spectra of PFC-700 and PFC-800 modified electrode, and (b) EIS of PFC-800 electrode before and after 1000 cycles.

with respect to PFC-700 electrode. It can be attributed to the enhancement in size of mesopores which in turn leads to increase of useable specific surface area and the decrease of diffusion resistance. Low R_{ct} value indicates a high rate of ions diffusion in active sites of an electrode. When charge transfer resistance is lowered, the electrolyte ions can readily diffuse into the pores of the electrode material and access the surface of active electrode material.

Fig. 8b presents Nyquist plots for PFC-800 before and after 10,000 cycles. Due to the decrease of specific capacitance at increased cycles, the R_{ct} value rises from 6 to $18 \Omega \text{ cm}^2$. The PFC-800 carbon material was found to be better for the supercapacitor performance while compared with other bio-waste derived carbons (Wang et al., 2015). This is because the chemical activation treatment can generate more amount of micro/mesopores, which leads to a larger specific surface area resulting in a significantly increased reaction area, and allowing for much better electrolyte penetration during the electrochemical reaction process. In addition, the CO_2 activation provides more functional groups on the carbon surface, thus leading to significant changes in the electron/donor characteristics and improvement of the wet ability of the carbon surface (Huang et al., 2012). These properties of the PFC electrode materials enhance the electrical conductivity, which would be beneficial for high-rate supercapacitor applications.

A list for comparing specific capacitance values among different electrodes is summarized in Table S1 in the Supporting Information along with their BET specific surface areas.

3.3. Removal of sunset yellow

In recent years, the development of industrialization accompanied by water pollution has attracted intensive concern (Aliabadi and Mahmoodi, 2018). Sunset yellow FCF (SY) has been popularly used in industries such as food, beverage, paper, leather, cosmetic, and textile (Sá et al., 2013; Gao et al., 2013a,b). Its chemical structure and physicochemical properties were displayed in Table S2 in the Supporting Information. It can cause allergy, dermatitis, diarrhea, and skin irritation, also provoke cancer, mutation and carcinogenic side effects in human (Mekawy et al., 1998; Zandipak and Sobhanardakani, 2016). However, its complex chemical structure may resist against light and oxidizing agents. Thus easily

causing contamination of environment and food chains. Therefore, azo dyes have been banned as food additives in food industry and carefully removed from the environment. However, the technologies such as coagulation/flocculation, chemical oxidation, filtration, chemical reduction, and photodegradation were found to reach limited success in the treatment of dye-containing wastewaters (Ghoneim et al., 2011; Chanderia et al., 2017; Huang et al., 2018a–c). In contrast, adsorption is considered to be the most effective technique for wastewater treatment, due to its simplicity, low cost, and high efficiency (Vasques et al., 2014; Huang et al., 2018a–c). To effectively remove organic dye pollutants from water, we adopt the PFC as an adsorbent for the adsorption performance for SY. Its high surface area, large pore size and pore volume should favor the adsorption process.

Accordingly, the Langmuir adsorption isotherms of PFC-700 and PFC-800 were given in details Supporting Information. Note that the PFC-800 yielded the largest adsorption capacity ($Q_0 = 273.6 \text{ mg g}^{-1}$) in examination of SY among those reported carbon-based adsorbents (Table S3 in the Supporting Information) such as MOFs/GO ($Q_0 = 81.28 \text{ mg g}^{-1}$; Li et al., 2016), MPMWCNT ($Q_0 = 85.47 \text{ mg g}^{-1}$; Gao et al., 2013a,b), lady finger stem ($Q_0 = 15.92 \text{ mg g}^{-1}$; Abbas et al., 2012) and mangrove barks ($Q_0 = 12.72 \text{ mg g}^{-1}$; Seey and Kassim, 2012). Fig. S1 in the Supporting Information shows the optical photographs of the PFC-800 adsorbent for SY before and after adsorption; the SY became colorless compared to the original solution. This could be attributed to its ultrahigh surface area, large pore volume, and oxygen-containing functional groups, such as $-\text{COOH}$ and $-\text{OH}$ on the pore channels and edges of PFC-800. Meanwhile, PFC-800 has a huge surface area and graphitized pore structure allowing strong $\pi-\pi$ interactions with the aromatic moieties present in the dye molecules (Veerakumar et al., 2017), thereby increasing the adsorption capacity of SY dyes. The BET isotherm of the SY dye adsorbed on PFC-800 was shown in Fig. S2, in the Supporting Information. It is noticed that the BET surface area of PFC-800 decreased with an increase of the dye adsorption. Some micropores could be blocked by the adsorbed pollutants, which caused the reduction of surface area and the corresponding textural properties for PFC-800 sample was depicted in Table S4, Supporting Information. These results make the PFC-800 a promising adsorbent

candidate for the treatment of wastewater containing organic food dyes.

4. Conclusions

We have prepared porous carbon materials from paper flower via a facile chemical and physical activation process and exploited its applications as electrode material for SC and dye removal. The morphology, structure, and textural properties of the as-prepared PFC were inspected by a variety of physicochemical techniques, revealing that PFC are in the form of thin sheets, which are folded showing an ultrathin sheet-like morphology with an area size in the range of few hundred nanometers. The CV curve of PFC is characteristic of a typical rectangular shape in agreement with its electric double-layer capacitive behavior. The porous carbon electrode (PFC-800) was found to have a high specific capacitance of 118 F g^{-1} at current density of 1 A g^{-1} and 91.2 F g^{-1} at higher current density of 12 A g^{-1} . In particular, the PFC-800 sample shows a long cycling life with excellent capacitance retention at 97.4% after 10,000 charge–discharge cycles. This may be due to the extraordinary micro/mesoporous nature with a high surface area ($S_{\text{BET}} = 1801\text{ m}^2\text{ g}^{-1}$); this porous nature leads to the formation of efficient EDLCs, indicating that it can be made a promising electrode material for electrochemical supercapacitors. Moreover, the maximum adsorption capacity for SY was calculated to be 273.6 mg g^{-1} , which is due the large surface area, hydrogen bonding, π - π electron, and electrostatic interactions.

Acknowledgements

The authors wish to thank the Department of Science and Technology-Science and Engineering Research Board (DST-SERB), Govt. of India, for financial support under the Early Career Research Award (ECRA) program (ECR/2016/002025). This work is supported by the Ministry of Science and Technology (MOST), Taiwan.

Appendix A. Supplementary material

Supplementary data associated with this article can be found, in the online version, at <https://doi.org/10.1016/j.arabjc.2018.08.009>.

References

- Abbas, A., Rehman, R., Murtaza, S., Shafique, U., Zahid, A., Ayub, R., 2012. Adsorptive removal of Congo red and sunset yellow dyes from water systems by lady finger stem. *J. Chem. Soc. Pak.* 34, 1241–1247.
- Aliabadi, R.S., Mahmoodi, N.O., 2018. Synthesis and characterization of polypyrrole, polyaniline nanoparticles and their nanocomposite for removal of azo dyes; Sunset yellow and congo red. *J. Clean. Prod.* 179, 235–245.
- Biswal, M., Banerjee, A., Deo, M., Ogale, S., 2013. From dead leaves to high energy density supercapacitors. *Energy Environ. Sci.* 6, 1249–1259.
- Borenstein, A., Hanna, O., Attias, R., Luski, S., Brousse, T., Aurbach, D., 2017. Carbon-based composite materials for supercapacitor electrodes: A review. *J. Mater. Chem. A* 5, 12653–12672.
- Chandera, K., Kumar, S., Sharma, J., Ameta, R., Punjabi, P.B., 2017. Degradation of sunset yellow FCF using copper loaded bentonite and H_2O_2 as photo-fenton like reagent. *Arabian J. Chem.* 10, S205–S211.
- Chen, L.-F., Lu, Y., Yu, L., Lou, X.W., 2017. Designed formation of hollow particle-based nitrogen-doped carbon nanofibers for high-performance supercapacitors. *Energy Environ. Sci.* 10, 1777–1783.
- Choi, D., Blomgren, G.E., Kumta, P.N., 2006. Fast and reversible surface redox reaction in nanocrystalline vanadium nitride supercapacitors. *Adv. Mater.* 18, 1178–1182.
- Das, H.T., Mahendraprabhu, K., Maiyalagan, T., Elumalai, P., 2017. Performance of solid-state hybrid energy-storage device using reduced graphene-oxide anchored sol-gel derived Ni/NiO nanocomposite. *Sci. Rep.* 7, 15432.
- Dominguez, J.C., Olliet, M., Alonso, M.V., Rojo, E., Rodriguez, F., 2013. Structural, thermal and rheological behavior of a bio-based phenolic resin in relation to a commercial resol resin. *Ind. Crops Prod.* 42, 308–314.
- Gao, H.J., Kanc, T.T., Zhao, S.Y., Qian, Y.X., Cheng, X.Y., Wu, W. L., Wang, X.D., Zheng, L.Q., 2013a. Removal of anionic azo dyes from aqueous solution by functional ionic liquid cross-linked polymer. *J. Hazard. Mater.* 261, 84–90.
- Gao, Y., Zhang, W., Yue, Q., Gao, B., Sun, Y., Kong, J., Zhao, P., 2014. Simple synthesis of hierarchical porous carbon from *Enteromorpha prolifera* by a self-template method for supercapacitor electrodes. *J. Power Sources* 270, 403–410.
- Gao, H.J., Zhao, S.Y., Cheng, X.Y., Wang, X.D., Zheng, L.Q., 2013b. Removal of anionic azo dyes from aqueous solution using magnetic polymer multi-wall carbon nanotube nanocomposite as adsorbent. *Chem. Eng. J.* 223, 84–90.
- Ghoneim, M.M., El-Desoky, H.S., Zidan, N.M., 2011. Electro-Fenton oxidation of sunset yellow FCF azo-dye in aqueous solutions. *Desalination* 274, 22–30.
- Gu, W., Wang, X., Yushin, G., 2015. Nanostructured activated carbons for supercapacitors. In: Feng, X. (Ed.), *Nanocarbons for Advanced Energy Storage*. Wiley-VCH, pp. 1–34.
- Guo, N., Li, M., Sun, X., Wang, F., Yang, R., 2017. Tremella derived ultrahigh specific surface area activated carbon for high performance supercapacitor. *Mater. Chem. Phys.* 201, 399–407.
- Halama, A., Szubzda, B., Pasciak, G., 2010. Carbon aerogels as electrode material for electrical double layer supercapacitors-synthesis and properties. *Electrochim. Acta* 55, 7501–7505.
- Han, J., Ge, J., Ren, Z., Tu, J., Sun, Z., Chen, S., Xie, G., 2017. Facile green synthesis of 3D porous glucose-based carbon aerogels for high-performance supercapacitors. *Electrochim. Acta* 258, 951–958.
- He, X., Ling, P., Yu, M., Wang, X., Zhang, X., Zheng, M., 2013. Rice husk-derived porous carbons with high capacitance by ZnCl_2 activation for supercapacitors. *Electrochim. Acta* 105, 635–641.
- Hsieh, C.T., Teng, H., 2002. Influence of oxygen treatment on electric double-layer capacitance of activated carbon fabrics. *Carbon* 40, 667–674.
- Hu, Z., Srinivasan, M.P., Ni, Y., 2001. Novel activation process for preparing highly microporous and mesoporous activated carbons. *Carbon* 39, 877–886.
- Huang, Y., Liang, J., Chen, Y., 2012. An overview of the applications of graphene-based materials in supercapacitors. *Small* 8, 1805–1834.
- Huang, Y., Liu, Z., Zhao, G., 2016. Reaction process for ZnCl_2 activation of phenol liquefied wood fibers. *RSC Adv.* 6, 78909–78917.
- Huang, Y., Li, K., Lin, Y., Tong, Y., Liu, H., 2018b. Enhanced efficiency of electron-hole separation in $\text{Bi}_2\text{O}_3\text{CO}_3$ for photocatalysis via acid treatment. *Chem Cat Chem* 10, 1982–1987.
- Huang, Y., Li, K., Li, S., Lin, Y., Liu, H., Tong, Y., 2018c. Ultrathin Bi_2MoO_6 nanosheets for photocatalysis: Performance enhancement by atomic interfacial engineering. *Chem. Select* 13, 7423–7428.

- Huang, Y., Xu, H., Yang, H., Lin, Y., Liu, H., Tong, Y., 2018a. Efficient charges separation using advanced BiOI-based hollow spheres decorated with palladium and manganese dioxide nanoparticles. *ACS Sustain. Chem. Eng.* 6, 2751–2757.
- Hwang, J.Y., Li, M., El-Kady, M.F., Kaner, R.B., 2017. Next-Generation activated carbon supercapacitors: A simple step in electrode processing leads to remarkable gains in energy density. *Adv. Funct. Mater.* 27, 1605745.
- Isah, K.U., Ahmadu, U., Idris, A., Kimpa, M.I., Uno, U.E., Ndamitso, M.M., 2015. Noble Alu Betalain pigments as natural photosensitizers for dye-sensitized solar cells: The effect of dye pH on the photoelectric parameters. *Mater. Renew. Sustain. Energy* 4, 39.
- Jayalakshmi, M., Balasubramanian, K., 2008. Simple capacitors to supercapacitors—An overview. *Int. J. Electrochem. Sci.* 3, 1196–1217.
- Jeong, H.M., Lee, J.W., Shin, W.H., Choi, Y.J., Shin, H.J., Kang, J. K., Choi, J.W., 2011. Nitrogen-doped graphene for high-performance ultracapacitors and the importance of nitrogen-doped sites at basal planes. *Nano Lett.* 11, 2472–2477.
- Jiang, D.B., Zhang, B.Y., Zheng, T.X., Zhang, Y.X., Xu, X., 2018. One-pot synthesis of g-Fe₂O₃ nanospheres/diatomite composites for electrochemical capacitor electrodes. *Mater. Lett.* 215, 23–26.
- Kang, X., Zhu, H., Wang, C., Sun, K., Yin, J., 2018. Biomass derived hierarchically porous and heteroatom-doped carbons for supercapacitors. *J. Colloid. Inter. Sci.* 509, 369–383.
- Karnan, M., Subramani, K., Sudhan, N., Ilayaraja, N., Sathish, M., 2016. Aloe vera derived activated high-surface-area carbon for flexible and high-energy supercapacitors. *ACS Appl. Mater. Interfaces* 8, 35191–35202.
- Khairy, M., Ismael, M., El-Khatib, R.M., Abdelnaeem, M., Khalaf, M., 2016. Natural betanin dye extracted from bougainvillea flowers for the naked-eye detection of copper ions in water samples. *Anal. Methods* 8, 4977–4982.
- Kinoshita, K., 1988. *Carbon: Electrochemical and Physicochemical Properties*. Wiley, New York.
- Knight, D.S., White, W.B., 1989. Characterization of diamond films by Raman spectroscopy. *J. Mater. Res.* 4, 385–393.
- Li, W.R., Chen, D.H., Li, Z., Shi, Y.F., Wan, Y., Wang, G., Jiang, Z. Y., Zhao, D.Y., 2007. Nitrogen-containing carbon spheres with very large uniform mesopores: the superior electrode materials for EDLC in organic electrolyte. *Carbon* 45, 1757–1763.
- Li, X., Ding, S., Xiao, X., Shao, J., Wei, J., Pang, H., Yu, Y., 2017. N, S co-doped 3D mesoporous carbon-Co₃Si₂O₅(OH)₄ architectures for high-performance flexible pseudo-solid-state supercapacitors. *J. Mater. Chem. A* 5, 12774–12781.
- Li, L., Shi, Z., Zhu, H., Hong, W., Xie, F., Sun, K., 2016. Adsorption of azo dyes from aqueous solution by the hybrid MOFs/GO. *Water. Sci. Technol.* 73, 1728–1737.
- Li, X., Xiao, X., Li, Q., Wei, J., Xue, H., Pang, H., 2018. Metal (M = Co, Ni) phosphate based materials for high-performance supercapacitors. *Inorg. Chem. Front.* 5, 11–28.
- Li, Z., Xu, Z., Tan, X., Wang, H., Holt, C.M.B., Stephenson, T., Olsen, B.C., Mitlin, D., 2013. Mesoporous nitrogen-rich carbons derived from protein for ultra-high capacity battery anodes and supercapacitors. *Energy Environ. Sci.* 6, 871–878.
- Long, C., Chen, X., Jiang, L., Zhi, L., Fan, Z., 2015. Porous layer-stacking carbon derived from in-built template in biomass for high volumetric performance supercapacitors. *Nano Energy* 12, 141–151.
- Lu, Y., Li, B., Zheng, S., Xu, Y., Xue, H., Pang, H., 2017. Syntheses and energy storage applications of M_xS_y (M = Cu, Ag, Au) and their composites: Rechargeable batteries and supercapacitors. *Adv. Funct. Mater.* 27, 1703949.
- Mekkiaw, H.A., Ali, M.O., El-Zawahry, A.M., 1998. OP3A18-Toxic effect of synthetic and natural food dyes on renal and hepatic functions in rats. *Toxicol. Lett.* 95 (Suppl. 1), 155.
- Panmand, R.P., Patil, P., Sethi, Y., Kadam, S.R., Kulkarni, M.V., Gosavi, S.W., Munirathnam, N.R., Kale, B.B., 2017. Unique perforated graphene derived from Bougainvillea flowers for high-power supercapacitors: A green approach. *Nanoscale* 9, 4801–4809.
- Peng, C., Yan, X.-B., Wang, R.-T., Lang, J.-W., Ou, Y.-J., Xue, Q.-J., 2013. Promising activated carbons derived from waste tea-leaves and their application in high performance supercapacitors electrodes. *Electrochim. Acta* 87, 401–408.
- Raj, B.G.S., Asiri, A.M., Wu, J.J., Anandan, S., 2015a. Synthesis of Mn₃O₄ nanoparticles via chemical precipitation approach for supercapacitor application. *J. Alloy. Compd.* 636, 234–240.
- Raj, B.G.S., Ramprasad, R.R., Asiri, A.M., Wu, J.J., Anandan, S., 2015b. Ultrasound assisted synthesis of Mn₃O₄ nanoparticles anchored graphene nanosheets for supercapacitor applications. *Electrochim. Acta* 156, 127–137.
- Ratha, S., Rout, C.S., 2013. Supercapacitor electrodes based on layered tungsten disulfide-reduced graphene oxide hybrids synthesized by a facile hydrothermal method. *ACS Appl. Mater. Interfaces* 5, 11427–11433.
- Rudge, A., Davey, J., Raistrick, I., Gottesfeld, S., Ferraris, J.P., 1994. Conducting polymers as active materials in electrochemical capacitors. *J. Power Sources* 47, 89–107.
- Sá, F.P.D., Cunha, B.N., Nunes, L.M., 2013. Effect of pH on the adsorption of sunset yellow FCF food dye into a layered double hydroxide (CaAl-LDH-NO₃). *Chem. Eng. J.* 215, 122–127.
- Seey, T.L., Kassim, M.J.N.M., 2012. Acidic and basic dyes removal by adsorption on chemically treated mangrove barks. *Int. J. Appl. Sci. Technol.* 2, 270–276.
- Sevilla, M., Fuertes, A.B., 2014. Direct synthesis of highly porous interconnected carbon nanosheets and their application as high performance supercapacitors. *ACS Nano* 8, 5069–5078.
- Shi, C., Hu, L., Guo, K., Li, H., Zhai, T., 2017. Highly porous carbon with graphene nanoplatelet microstructure derived from biomass waste for high-performance supercapacitors in universal electrolyte. *Adv. Sustain. Syst.* 1, 1600011.
- Shi, Y., Peng, L., Ding, Y., Zhao, Y., Yu, G., 2015. Nanostructured conductive polymers for advanced energy storage. *Chem. Soc. Rev.* 44, 6684–6696.
- Tian, Q., Wang, X., Xu, X., Zhang, M., Wang, L., Zhao, X., An, Z., Yao, H., Gao, J., 2018. A novel porous carbon material made from wild rice stem and its application in supercapacitors. *Mater. Chem. Phys.* 213, 267–276.
- Vasques, É.C., Carpiné, D., Dagostin, J.L.A., Canteli, A.M.D., Igarashi-Mafra, L., Mafra, M.R., Scheer, A.P., 2014. Modelling studies by adsorption for the removal of sunset yellow azo dye present in effluent from a soft drink plant. *Environmen. Technol.* 35, 1532–1540.
- Veerakumar, P., Jeyapragasam, T., Ramakrishnan, M., Panneer Muthuselvam, I., Lin, K.-C., 2017. Graphene oxide nanosheets as an efficient and reusable sorbents for eosin yellow dye removal from aqueous solutions. *Chem. Select* 2, 3598–3607.
- Veerakumar, P., Rajkumar, C., Chen, S.-M., Thirumalraj, B., Lin, K.-C., 2018. Activated porous carbon supported rhenium composites as electrode materials for electrocatalytic and supercapacitor applications. *Electrochim. Acta* 271, 433–447.
- Wahid, M., Puthusseri, D., Phase, D., Ogale, S., 2014. Enhanced capacitance retention in a supercapacitor made of carbon from sugarcane bagasse by hydrothermal pretreatment. *Energy Fuels* 28, 4233–4240.
- Wang, D., Geng, Z., Li, B., Zhang, C., 2015. High performance electrode materials for electric double-layer capacitors based on biomass-derived activated carbons. *Electrochim. Acta* 173, 377–384.
- Wang, J., Kaskel, S., 2012. KOH activation of carbon-based materials for energy storage. *J. Mater. Chem.* 22, 23710–23725.
- Wang, H., Xu, Z., Kohandehghan, A., Li, Z., Cui, K., Tan, X., Stephenson, T.J., Kingodu, C.K., Holt, C.M.B., Olsen, B.C., Tak, J.K., Harfield, D., Anyia, A.O., Mitlin, D., 2013. Interconnected

- carbon nanosheets derived from hemp for ultrafast supercapacitors with high energy. *ACS Nano* 7, 5131–5141.
- Wei, L., Sevilla, M., Fuertes, A.B., Mokaya, R., Yushin, G., 2011. Hydrothermal carbonization of abundant renewable natural organic chemicals for high-performance supercapacitor electrodes. *Adv. Energy Mater.* 1, 356–361.
- Yahya, M.A., Al-Qodah, Z., Ngah, C.W.Z., 2015. Agricultural biowaste materials as potential sustainable precursors used for activated carbon production: A review. *Renew. Sustain. Energy Rev.* 46, 218–235.
- Yang, H., Kannappan, S., Pandian, A.S., Jang, J.-H., Lee, Y.S., Lu, W., 2017. Graphene supercapacitor with both high power and energy density. *Nanotechnology* 28, 445401.
- Yao, Y., Zhang, Y., Li, L., Wang, S., Dou, S., Liu, X., 2017. Fabrication of hierarchical porous carbon nanoflakes for high performance supercapacitors. *ACS Appl. Mater. Interfaces* 9, 34944–34953.
- Yu, X., Tang, Z., Sun, D., Ouyang, L., Zhu, M., 2017. Recent advances and remaining challenges of nanostructured materials for hydrogen storage applications. *Progress Mater. Sci.* 88, 1–48.
- Yu, X., Wang, S., Zhang, J., 2018. Preparation of high adsorption performance activated carbon by pyrolysis of waste polyester fabric. *J. Mater. Sci.* 53, 5458–5466.
- Zaaba, N.I., Foo, K.L., Hashim, U., Tan, S.J., Liu, W.-W., Voon, C. H., 2017. Synthesis of graphene oxide using modified hummers method solvent influence. *Procedia Eng.* 184, 469–477.
- Zandipak, R., Sobhanardakani, S., 2016. Synthesis of NiFe_2O_4 nanoparticles for removal of anionic dyes from aqueous solution. *Desalin. Water Treat.* 57, 11348–11360.
- Zhang, X., Lin, Q., Luo, S., Ruan, K., Peng, K., 2018. Preparation of novel oxidized mesoporous carbon with excellent adsorption performance for removal of malachite green and lead ion. *Appl. Surf. Sci.* 442, 322–331.
- Zhang, P., Sun, F., Shen, Z., Cao, D., 2014. ZIF-derived porous carbon: A promising supercapacitor electrode material. *J. Mater. Chem. A* 2, 12873–12880.
- Zhang, Y., Zhang, Y., Huang, J., Du, D., Xing, W., Yan, Z., 2016. Enhanced capacitive performance of N doped activated carbon from petroleum coke by combining ammoxidation with KOH activation. *Environ. Sci. Pollut. Res.* 23, 128–138.
- Zhang, L.L., Zhao, X.S., 2009. Carbon-based materials as supercapacitor electrodes. *Chem. Soc. Rev.* 38, 2520–2531.
- Zhang, L., Zheng, S., Wang, L., Tang, H., Xue, H., Wang, G., Pang, H., 2017. Fabrication of metal molybdate micro/nanomaterials for electrochemical energy storage. *Small* 13, 1700917.
- Zhao, L., Fan, L.-Z., Zhou, M.-Q., Guan, H., Qiao, S., Antonietti, M., Titirici, M.M., 2010. Nitrogen-containing hydrothermal carbons with superior performance in supercapacitors. *Adv. Mater.* 22, 5202–5206.
- Zheng, S., Xue, H., Pang, H., 2017. Supercapacitors based on metal coordination materials. *Coordination Chem. Rev.* <https://doi.org/10.1016/j.ccr.2017.07.002>.
- Zhou, L., Cao, H., Zhu, S., Hou, L., Yuan, C., 2015. Hierarchical micro-/mesoporous N-and O-enriched carbon derived from disposable cashmere: A competitive cost-effective material for high-performance electrochemical capacitors. *Green Chem.* 17, 2373–2382.
- Zhu, S., Li, L., Liu, J., Wang, H., Wang, T., Zhang, Y., Zhang, L., Ruoff, R.S., Dong, F., 2018. Structural directed growth of ultrathin parallel birnessite on $\beta\text{-MnO}_2$ for high-performance asymmetric supercapacitors. *ACS Nano* 12, 1033–1042.
- Zickler, G.A., Smarsly, B., Gierlinger, N., Peterlik, H., Paris, O., 2006. A reconsideration of the relationship between the crystallite size L_a of carbons determined by X-ray diffraction and Raman spectroscopy. *Carbon* 44, 3239–3246.